J. Fluid Mech. (2014), *vol.* 738, *pp.* 105–123. © Cambridge University Press 2013
doi:10.1017/jfm.2013.532

Spatial simulation of channel flow instability and control

Alec Kucala and Sedat Biringen†

Department of Aerospace Engineering Sciences, University of Colorado, Boulder, CO 80309, USA

(Received 10 December 2012; revised 16 August 2013; accepted 2 October 2013;
first published online 4 December 2013)

A direct numerical simulation is performed on the full time-dependent three-dimensional Navier–Stokes equations in a spatially developing plane-channel flow at a Reynolds number of 10 000. Two-dimensional eigenfunctions based on the solution of the Orr–Sommerfeld equation are introduced at the inflow with random noise added to simulate a vibrating ribbon transition experiment. The flow is allowed to choose a natural path to secondary instability, either K-type (after Klebanoff) or H-type (after Herbert), depending on the amplitude of the two-dimensional disturbance. For low-amplitude two-dimensional disturbances (1 % of the centreline velocity), H-type modes are found to dominate, while a doubling of the amplitude (2 % of the centreline velocity) produces a mixed H-type/K-type disturbance field with explosive growth of the secondary modes. In addition, the use of a suction/blowing slot that is phase lagged with respect to a fixed wall pressure signal is demonstrated to significantly reduce the energy in the primary mode owing to the destruction of phase between the streamwise and wall-normal velocity components. The use of forward finite-time Lyapunov exponents to generate Lagrangian coherent structures as a means of flow visualization is also presented, showing qualitative agreement with previous experimental visualizations, and represents a viable means of identifying characteristic vortical flow structures.

Key words: flow control, instability control, nonlinear instability

1. Introduction

A common path to transition from laminar to turbulent flow in plane-channel and boundary-layer flows occurs when an initially two-dimensional (primary) instability, also known as the Tollmien–Schlichting (TS) wave, becomes susceptible to three-dimensional disturbances at some finite amplitude. This is known as the secondary instability and is characterized by the appearance of either K-type or H-type disturbance patterns. K-type instabilities (after Klebanoff) were first observed in the ground-breaking boundary-layer experiments of Klebanoff, Tidstrom & Sargent (1962), and later in plane-channel flow experiments by Nishioka, Asai & Iida (1980). These are characterized by Λ-shaped structures (Λ vortices) arranged in a distinctive pattern periodic in the streamwise (x) and spanwise (z) directions such that $x \rightarrow x + \lambda_x$ and $z \rightarrow z + \lambda_z$, where λ_x is the streamwise wavelength of the primary (TS) instability and λ_z is the spanwise wavelength of the secondary instability.

† Email address for correspondence: biringen@colorado.edu

https://doi.org/10.1017/jfm.2013.532 Published online by Cambridge University Press

As an alternative path to secondary instability, Herbert theoretically predicted the onset of subharmonic modes in both channel flows (Herbert 1983) and boundary layers (Herbert 1988) for low two-dimensional amplitudes; Herbert's theory also predicted a mixing of fundamental and subharmonic modes for higher two-dimensional amplitudes. The subharmonic mode is labelled as H-type (after Herbert) and is characterized by a staggered arrangement of Λ vortices invariant to coordinate transformations of the type $x \rightarrow x + 2\lambda_x$ and $z \rightarrow z + \lambda_z$, and by the combined shift $(x, z) \rightarrow (x + \lambda_x, z + \lambda_z/2)$. That is, the subharmonic secondary instability has a streamwise wavelength λ_x that is twice the length of the primary TS wave. The existence of H-type (subharmonic) instability was confirmed in the boundary-layer experiments of Kachanov, Kozlov & Levchenko (1978), Kachanov & Levchenko (1984) and Saric, Kozlov & Levchenko (1984). In a more recent experimental study considering boundary-layer flow with adverse pressure gradient (Borodulin, Kachanov & Koptsev 2002), a large band of subharmonic and harmonic modes were found to amplify with random noise, with and without the primary TS wave being forced at the inflow.

The existence of H- and K-type instability was also captured in temporal direct numerical simulations in doubly periodic domains (May & Kleiser 1985; Spalart & Yang 1987; Singer, Reed & Ferziger 1989). In these studies, several discrepancies between computational and experimental studies were observed. For example, the boundary-layer simulations of Spalart & Yang (1987) did not reveal the existence of pure K-type instability at large two-dimensional amplitudes; instead, a mixture of H- and K-type instabilities was detected. This is in contrast with the experiments of Saric *et al.* (1984), which clearly identified the formation of K-type structures.

In a similar vein, the direct simulations of Singer (1987) and Singer *et al.* (1989) obtained a mixture of H- and K-type instability with high-amplitude initial two-dimensional disturbances, whereas in the channel flow experiments of Nishioka *et al.* (1980), secondary instability was observed to be pure K-type. Furthermore, channel flow experiments have not revealed H-type instability except in the presence of a forced subharmonic (Ramazanov 1985), while computations (May & Kleiser 1985; Singer 1987; Singer *et al.* 1989) and theory (Herbert 1983) predict the evolution of H-type secondary instability for low two-dimensional excitation amplitudes.

The present study follows the temporal direct numerical simulation conducted by Singer (1987), Kim & Moser (1989) and Singer *et al.* (1989) in a spatially evolving numerical simulation to assess the dominance of either subharmonic or fundamental instability in the path to natural transition. In this paper we define the modes as multiples of the real fundamental frequency ω_r and real spanwise wavenumber $\beta_r = 2\pi/L_z$ such that $\omega = n\omega_r$ and $\beta = m\beta_r$. Every mode can then be expressed as a pair (n, m), the primary mode being $(1, 0)$. To replicate the vibrating ribbon commonly used in laboratory experiments, the inflow conditions consist of the superposition of a two-dimensional primary TS wave with low-amplitude random noise allowing the growth of the fundamental $(1, m)$, or subharmonic $(0.5, m)$ modes, depending on the amplitude of the primary wave in a spatially evolving channel.

Control of these H- or K-type instabilities was initiated through a spanwise-homogeneous suction/blowing slot located at a fixed streamwise location in the channel in order to reduce the amplitude of the primary TS wave, thus delaying transition. This method of transition delay, proposed by Biringen (1984), has been demonstrated to reduce the growth of the TS wave in both experiments (Baumann & Nitsche 1996; Erdmann *et al.* 2011) and computations (Danabasoglu, Biringen & Streett 1991). Similarly, the computational work of Choi, Moin & Kim (1994) and Chang, Collis & Ramakrishnan (2002) employed opposition control in fully turbulent

https://doi.org/10.1017/jfm.2013.532 Published online by Cambridge University Press

periodic channel flows, obtaining approximately 20 % reduction in turbulent drag. Opposition control samples the wall-normal velocity at some sensing plane above the wall and prescribes an opposing wall-normal velocity through a suction/blowing slot located on the wall. Erdmann *et al.* (2011) demonstrated the applicability of opposition control in two-dimensional boundary-layer transition using an actuating membrane, which reduced the amplitude of the primary TS wave by almost 90 %. In this case, measurements of the velocity perturbations were made using a hot-wire anemometer, which allowed for the proper 'tuning' of the control signal for the reduction in the TS wave. In the control cases presented in this paper, the control signal will be tuned using a wall-pressure measurement upstream of the control slot, as opposed to the wall-normal velocity.

2. Numerical method

The full nonlinear time-dependent three-dimensional Navier–Stokes equations are solved in a spatially developing channel flow using a fractional step method (Waggy, Biringen & Sullivan 2013). With all spatial coordinates non-dimensionalized by the channel half-height δ and velocities by the centreline velocity U_c, the Navier–Stokes equations read (in conservative form)

$$\frac{\partial u_i}{\partial x_i} = 0, \tag{2.1}$$

$$\frac{\partial u_i}{\partial t} + \frac{\partial u_j u_i}{\partial x_j} = -\frac{\partial p}{\partial x_i} + \frac{1}{Re}\frac{\partial u_i}{\partial x_j x_j}, \tag{2.2}$$

where $Re = U_c\delta/\nu$, ν is the kinematic viscosity and the vector $\boldsymbol{u} = \langle u, v, w\rangle$ is composed of three velocity components in the x (streamwise), y (wall-normal) and z (spanwise) directions, respectively. Also, p represents non-dimensionalized pressure and t represents non-dimensionalized time.

The spatial derivatives are computed using fourth-order central differences, where the vertical diffusion terms are solved implicitly and the rest of the terms are solved explicitly. Hence the time integration is a semi-implicit Adams–Bashforth/Crank–Nicolson type method, which makes the numerical procedure second-order accurate in time. The streamwise (u) and spanwise (w) velocity components are discretized on a 'centred' vertical mesh, while the wall-normal (v) velocity component is discretized on a 'staggered' vertical mesh to enhance coupling between the vertical velocity and the pressure (Waggy *et al.* 2013). The flow geometry is shown in figure 1. In (2.1) and (2.2), the velocity vector can be decomposed into a base $\boldsymbol{u}_b$ and a fluctuating component $\boldsymbol{u}'$ such that

$$\boldsymbol{u} = \boldsymbol{u}_b + \boldsymbol{u}'. \tag{2.3}$$

Using the definition of velocity presented in (2.3), the initial/boundary conditions can be written as

$$\boldsymbol{u}_b(x = 0,\, 0 \leqslant y \leqslant 2,\, z) = \langle 1 - (1 - y)^2,\, 0,\, 0\rangle, \tag{2.4a}$$

$$\boldsymbol{u}'(x = 0,\, y,\, z,\, t) = A_{2D}\,\mathrm{Re}[\boldsymbol{u}_{e2D}(z)\mathrm{e}^{-\mathrm{i}\omega_r t}] + \boldsymbol{u}_r(y, z, t), \tag{2.4b}$$

$$\boldsymbol{u}(x, y = 0,\, 2,\, z) = 0, \tag{2.4c}$$

where A_{2D} is the amplitude of the two-dimensional disturbance and $\boldsymbol{u}_r$ is a vector field of random noise imposed at the inflow. The amplitude of each component in the random vector field is bounded by A_r and is uniformly distributed in wave

https://doi.org/10.1017/jfm.2013.532 Published online by Cambridge University Press

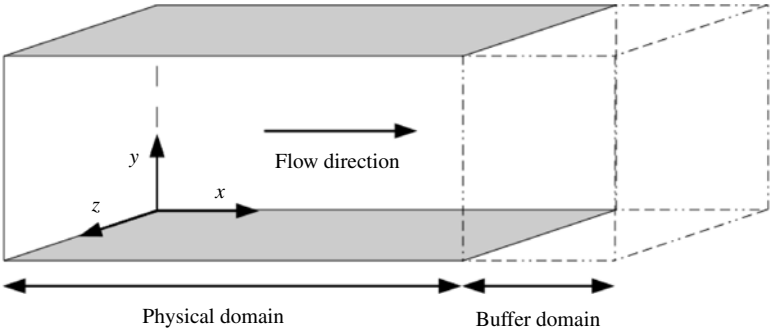


FIGURE 1. Flow geometry and coordinate system for the present channel flow simulation.

space such that there is no wavenumber biasing at the inflow. In addition, $\mathrm{i} = \sqrt{-1}$, ω_r is the prescribed real frequency for the solutions of the spatial modes of the Orr–Sommerfeld equation (Reynolds 1969), and $\boldsymbol{u}_{e2D}$ is the corresponding two-dimensional eigenfunction. Also (2.4*a*) is the laminar solution for plane Poiseuille flow, where the channel height spans from 0 to 2δ. For the present simulations, the mass flux is constant throughout the entire domain, as the eigenfunctions themselves explicitly preserve mass flow at the inflow for all times, owing to the negative symmetry of the streamwise perturbation velocity about the channel centreline. Therefore, at all times, the mass flux is held constant at the inflow boundary, providing a realistic model for comparison with experimental data (Barkley 1990).

The outflow boundary conditions for the spatially evolving (non-periodic) channel flow are modelled as a buffer domain appended to the computational domain (figure 1). In the buffer domain, the streamwise perturbation convective and viscous terms in the momentum equation, as well as the right-hand side of the pressure equation, are smoothly reduced to zero using a hyperbolic tangent function (Danabasoglu *et al.* 1991; Saiki *et al.* 1993). Periodic boundary conditions are applied in the spanwise (z) direction.

For active control cases, the no-slip boundary condition in (2.4*c*) is modified to include

$$\boldsymbol{u}(x_s \leqslant x \leqslant x_e, y = 0, 2, z) = \langle 0, A_c \cos(\omega_r t + \phi), 0 \rangle, \tag{2.5}$$

where x_s represents the front edge of the suction/blowing slot, x_e represents the back edge of the slot and ϕ represents the phase angle, which determines the phase of the control wave. The slot extends along the width of the channel in the spanwise direction, ensuring that the control signal is purely two-dimensional. Finally, A_c is the amplitude of the control wave, and can be varied depending on the amplitude of the wall-normal velocity component of the primary TS wave in accordance with Biringen (1984).

2.1. *Comparisons with linear theory*

To assess the accuracy and establish confidence in the present solution method, comparisons between linear theory for both two- and three-dimensional disturbances for a Reynolds number $Re = 10\,000$ are presented. At this Reynolds number, real frequency $\omega_r = 0.22$ and $\beta_r = \pm 1$ (three-dimensional case), the solution of the Orr–Sommerfeld equation (Reynolds 1969) obtains the complex eigenvalues $\alpha_{2D} = 0.9487 - 0.0123\mathrm{i}$ and $\alpha_{3D} = 0.7730 + 0.0277\mathrm{i}$ for the two- and three-dimensional

https://doi.org/10.1017/jfm.2013.532 Published online by Cambridge University Press

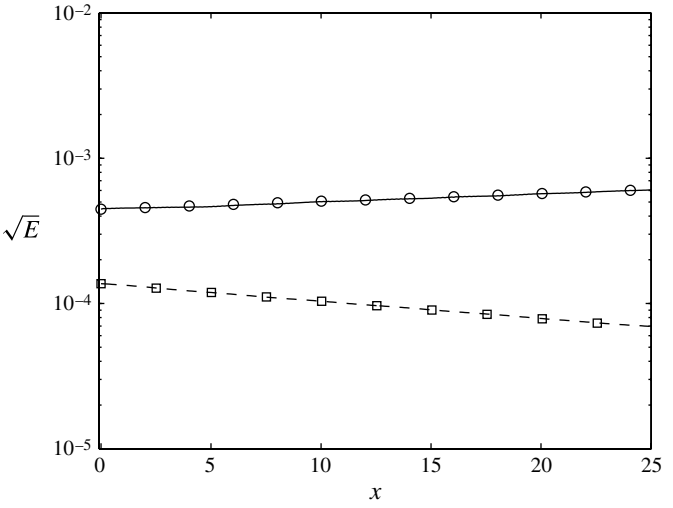


FIGURE 2. Spatial evolution of the (1, 0) (solid line) and (1, 1) (dashed line) modes for the two- and three-dimensional disturbances, respectively: ○, two-dimensional linear theory; □, three-dimensional linear theory.

disturbances, respectively. The value of ω_r was chosen such that it yields the least stable eigenvalue for $Re = 10\,000$ for two-dimensional disturbances. The corresponding spatial eigenfunctions of the Orr–Sommerfeld equation are introduced at inflow with real frequency ω_r and real spanwise wavenumber β_r. For both the two- and three-dimensional cases, approximately 60 grid points per TS wavelength were used in the streamwise direction, and 64 grid points per wavelength were used in the spanwise direction. At the inflow, the maximum amplitude of the two- and three-dimensional disturbances were 0.1 % of U_c. The time step was chosen such that the maximum Courant–Friedrichs–Lewy (CFL) number remained on the order of 10^{-1} and resolves each TS period into roughly 2000 time steps.

Modal distributions of the wall-integrated kinetic energy (see (3.1) in § 3.1) are used as a metric to measure the spatial growth rates of the low-amplitude inflow disturbances. These distributions, presented in figure 2, display excellent agreement with the linear theory, with a maximum deviation of 0.05 % (two-dimensional) and 0.48 % (three-dimensional), measured approximately four TS wavelengths downstream of the inflow. Hence, these results establish confidence in the present numerical method to accurately predict the spatial growth rates of two- and three-dimensional disturbances.

3. Results and discussion

3.1. *Modal evolution of secondary instability*

The flow parameters $Re = 10\,000$ and $\omega_r = 0.22$ were chosen to closely duplicate the conditions of the temporal simulation of Kim & Moser (1989), where the frequency has been selected such that the least stable primary mode is amplified. The amplitudes of the inflow disturbances are $A_{2D} = 0.01U_c$ and $A_{2D} = 0.02U_c$ and are referred to as the low-amplitude (LA) and high-amplitude (HA) cases, respectively. In both cases, the amplitude of the random disturbance, $A_r = 0.001U_c$, is set to simulate a 'natural'

https://doi.org/10.1017/jfm.2013.532 Published online by Cambridge University Press

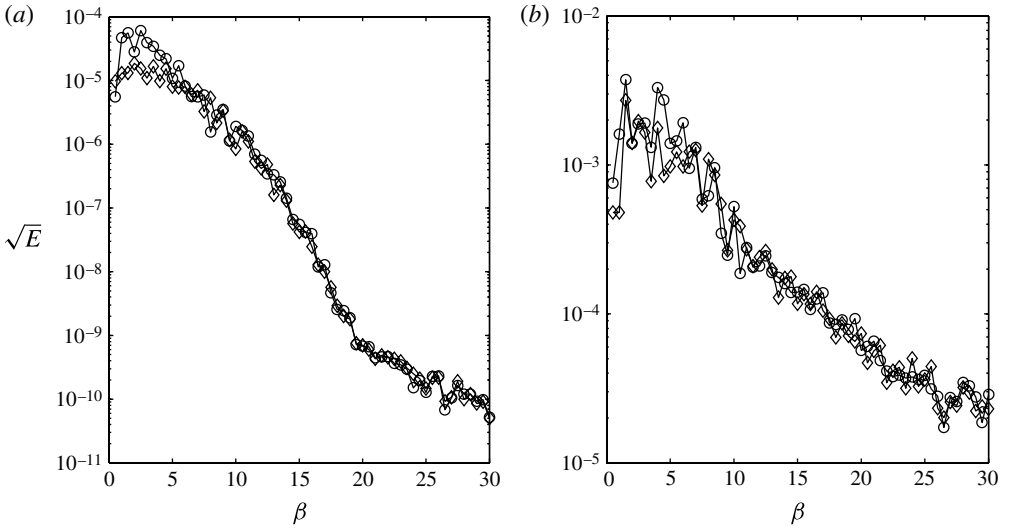


FIGURE 3. Spectrum of vertically averaged kinetic energy at $x = 55.80$ for (a) case LA and (b) case HA: ○, $\omega = 0.5$ (subharmonic); ◇, $\omega = 1$ (fundamental).

Case	A_{2D}	A_r	$N_x \times N_y \times N_z$
LA	$0.01U_c$	$0.001U_c$	$696 \times 65 \times 128$
HA	$0.02U_c$	$0.001U_c$	$696 \times 97 \times 128$

TABLE 1. Computational parameters for $Re = 10\,000$ and $\omega_r = 0.22$.

disturbance environment (Singer *et al.* 1989), where a wide spectrum of unbiased modes might be present at the inflow.

For the results that follow, the physical domain lengths are $L_x = 55\delta$, $L_y = 2\delta$ and $L_z = 4\pi\delta$. The streamwise physical domain length is chosen such that the inflow conditions will allow for the development of distinct K- or H-type disturbance patterns, where the buffer domain extends from $55 \leqslant x \leqslant 75$ and encompasses approximately 26 % of the total channel length. A summary of the computational parameters is provided in table 1.

Spectra of vertically averaged perturbation kinetic energy per unit mass,

$$E = \frac{1}{2}\int_0^2 (u'^2 + v'^2 + w'^2)\,\mathrm{d}y, \tag{3.1}$$

for the LA and HA cases, are presented in figures 3(a) and 3(b), respectively, at $x = 55.80$. In these figures, energy in the primary two-dimensional mode $(1, 0)$ was removed, allowing only the observation of the three-dimensional modes to determine K- or H-type dominance. The kinetic energy spectra were obtained over two full periods, $T_{TS} = 2\pi/\omega_r$, of the primary disturbance to capture the fundamental and the subharmonic modes. For both the LA and HA cases, the amplitudes in the subharmonic ($\omega = 0.5$) and fundamental modes ($\omega = 1$) decrease logarithmically with increasing spanwise wavenumber β. For the LA case, the subharmonic modes

https://doi.org/10.1017/jfm.2013.532 Published online by Cambridge University Press

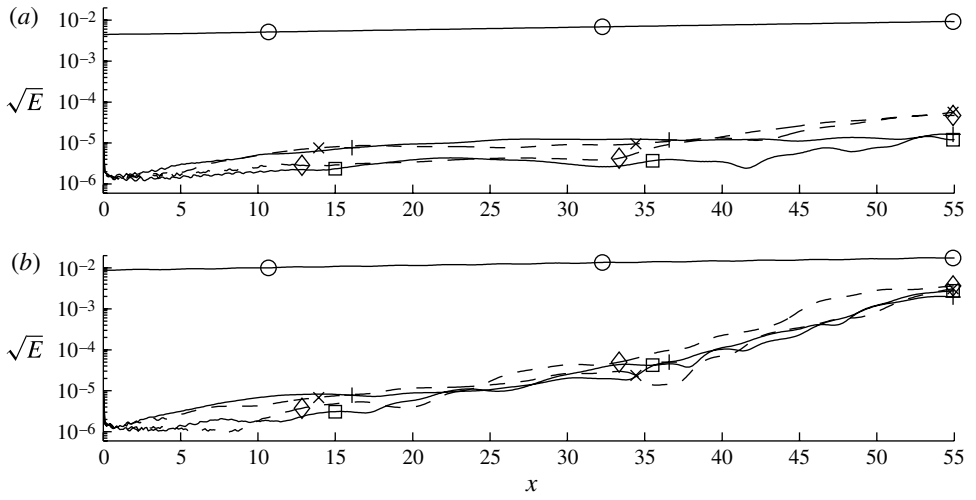


FIGURE 4. Streamwise evolution of vertically averaged kinetic energy for specific modes for two cases. (*a*) Case LA: ∘, (1, 0); ⋄, (0.5, 1); ×, (0.5, 2.5); □, (1, 1); +, (1, 2.5). (*b*) Case HA: ∘, (1, 0); ⋄, (0.5, 1.5); ×, (0.5, 4); □, (1, 1.5); +, (1, 4). Solid lines represent fundamental modes, while dashed lines represent subharmonic modes.

are about an order of magnitude higher in amplitude for spanwise wavenumbers $0.5 \leqslant \beta \leqslant 4$ when compared with the fundamental modes, indicative of H-type dominance in the largest scales. The higher spanwise wavenumbers do not show the same separation, as the energy transfer mechanisms that determine either K-type or H-type instability occur at the larger scales. For the HA case, there is evidence of mixed modes at low wavenumbers, where the subharmonic and fundamental modes are approximately of the same amplitude. Consequently, it can be inferred that, for the LA case, there is dominance of H-type instability, whereas the HA case is characterized by mixed modes at the lower spanwise wavenumbers, showing no dominance of K-type or H-type instability.

The streamwise evolution of the energy-containing modes for the LA and HA cases is presented in figures 4(*a*) and 4(*b*), respectively. For the LA case, the two-dimensional mode (1, 0) grows exponentially, as predicted by the linear theory. For $x \geqslant 40$ the subharmonic modes (0.5, 1) and (0.5, 2.5) have higher amplitudes than their fundamental counterparts, indicating H-type dominance, in agreement with the observations of Herbert (1983) and Singer *et al.* (1989). It is also evident that modal energy amplification is of the order $O(10^1)$ throughout the computational domain. There is, however, a competition between the fundamental (solid lines) and subharmonic (dashed lines) modes from $0 \leqslant x \leqslant 40$, where the amplitudes of the two modes are comparable for a given spanwise wavenumber β. As the disturbances travel downstream, the H-type modes are preferentially excited and become dominant.

Figure 5 shows the growth rate σ as a function of the spanwise wavenumber β for the LA case. The maximum growth of the subharmonic mode occurs at $\beta = 1.5$, roughly corresponding to the maximum growth rate calculated by Herbert (1983), $\beta = 1.26$. This discrepancy can be attributed to the finite length of the periodic spanwise domain $L_z = 4\pi\delta$, which yields wavenumbers as multiples of 0.5. In addition, an approximately linear decay in the growth rate with increasing β is observed in figure 5, comparable to Herbert's (1983) analysis for H-type instability.

https://doi.org/10.1017/jfm.2013.532 Published online by Cambridge University Press

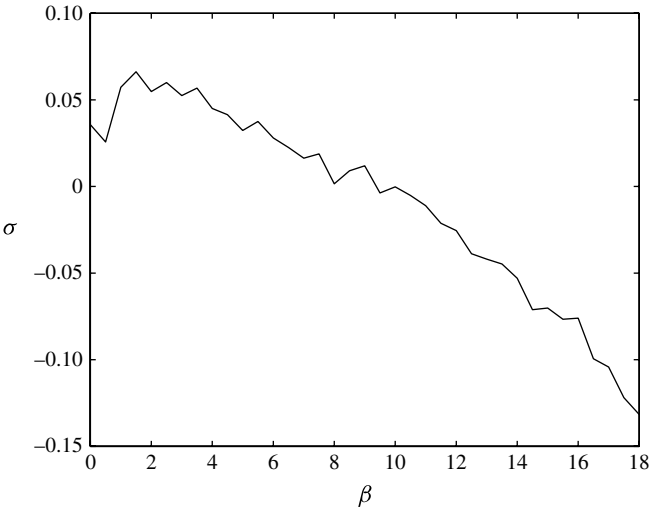


FIGURE 5. Growth rate σ of the subharmonic mode as a function of the spanwise wavenumber β measured at the end of the channel.

For the HA case (figure 4*b*), there is competition between the fundamental (solid lines) and subharmonic (dashed lines) modes similar to that observed for the LA case. However, here there is no clear preferential excitement of the subharmonic modes, and the fundamental modes increase at about the same rate as the subharmonic modes, leading to the presence of detuned (mixed) modes for $0 \leqslant x \leqslant 35$. In addition, the magnitude of energy in the three-dimensional modes has grown by approximately $O(10^3)$, i.e. much more rapidly than the LA case, although the two-dimensional amplitude A_{2D} is only a factor of two larger. This observation is similar to that of Kim & Moser (1989), that is, once the primary mode reaches a certain 'threshold' amplitude, rapid growth in the three-dimensional modes is excited.

Despite the presence of mixed modes at higher two-dimensional amplitudes, the H-type modes still dominate for approximately $x \geqslant 40$, in contrast to the experimental observations of Nishioka, Iida & Ichikawa (1975), where fundamental modes have higher amplitude. This discrepancy has also been observed in the temporal simulations of Singer *et al.* (1989), which they attributed to the presence of streamwise vorticity in the experiments of Nishioka *et al.* (1975). That is, in temporal simulations where H-type modes were found to dominate, the introduction of streamwise vortices in the initial conditions yielded K-type dominated modes.

It is important to note that the three-dimensional random disturbances imposed at the inflow for the present simulations follow closely the initial conditions imposed by Kim & Moser (1989), where no coherent streamwise vorticity is initially present. However, the natural evolution of secondary instability in Kim & Moser (1989) yielded K-type dominated modes for low amplitudes, where the present work yields H-type modes. Kim & Moser (1989) assert that, in a transition experiment where a two-dimensional wave is introduced (e.g. a vibrating magnetic ribbon) in the presence of rather small spanwise distortions in the mean flow, K-type modes should dominate whereas the theory would predict H-type modes. In the present work, the small spanwise distortions in the mean flow, caused by the random disturbance field at the inflow, do not induce a K-type secondary instability.

https://doi.org/10.1017/jfm.2013.532 Published online by Cambridge University Press

However, in Kim & Moser (1989) all of the Fourier modes were initially forced at the same amplitudes, whereas in the present study the two-dimensional mode is forced at a higher amplitude than the spanwise modes (see figure 4). This may provide an explanation for why Singer *et al.* (1989) and the present work did not display K-type dominance for low amplitudes where Kim & Moser (1989) show the opposite, and that coherent streamwise vorticity must be the catalyst for K-type breakdown in the presence of two-dimensional forcing. However, for 'natural' transition, where a wave packet containing a continuous spectrum of all Fourier modes is introduced, the natural evolution of the initially low-amplitude disturbances should exhibit K-type secondary instability once the primary mode reaches a threshold amplitude (Kim & Moser 1989).

3.2. *Flow visualization using Lagrangian coherent structures*

Lagrangian coherent structures (LCS) are defined as ridges in forward finite-time Lyapunov exponent (FTLE) fields. LCS represent barriers to transport (Shadden, Lekien & Marsden 2005) and can be used to identify vortex boundaries for a visual characterization of the flow field. While LCS have been used as a visualization tool in a variety of flow fields (Voth, Haller & Gollub 2002; Shadden *et al.* 2009; Lipinski & Mohseni 2010), they have not been deployed to identify the coherent structures characteristic of the early stages of transition (Λ vortices) reported in numerous experimental (Klebanoff *et al.* 1962; Kruse & Wagner 1998) and numerical (Singer *et al.* 1989; Zang & Krist 1989; Saiki *et al.* 1993) studies. In the present work, we have implemented this method for the high-amplitude case to visualize the coherent structures present in secondary instability during laminar–turbulent transition.

In a transition simulation it is possible to trace vortex lines or plot isocontours of vorticity to visually characterize the Λ vortices present in a secondary instability transition study. Generation of vortex lines, in particular, is sensitive to their spanwise placement of origin. LCS obtained from FTLE fields, in contrast, do not rely on the direct calculation of vorticity from discrete velocity data. Instead, one can take an existing set of Eulerian discrete velocity fields (in both time and space) and advect particles in a Lagrangian fashion to generate the FTLE. The FTLE is rather insensitive to the accuracy of the velocity field data (Haller 2002), which is an advantage for this particular simulation, owing to the noisy inflow conditions, which make traditional techniques less than ideal for observing coherent structures. However, the FTLE is sensitive to the integration time τ, and, with proper adjustment, coherent structures may be observed regardless of the noise level in the data. The FTLE is defined as

$$\Phi_T^{T+\tau}(\boldsymbol{x}) = \boldsymbol{x}(T) + \int_T^{T+\tau} \boldsymbol{v}(\boldsymbol{x}(t))\,\mathrm{d}t, \tag{3.2a}$$

$$\boldsymbol{\Delta} = \left(\frac{\mathrm{d}\Phi}{\mathrm{d}\boldsymbol{x}}\right) * \left(\frac{\mathrm{d}\Phi}{\mathrm{d}\boldsymbol{x}}\right), \tag{3.2b}$$

$$\sigma_T^{\tau}(\boldsymbol{x}) = \frac{1}{\tau} \ln \sqrt{\gamma_{max}(\boldsymbol{\Delta})}, \tag{3.2c}$$

where σ is the FTLE and $\gamma_{max}(\boldsymbol{\Delta})$ is the maximum eigenvalue of the Cauchy–Green deformation tensor $\boldsymbol{\Delta}$, which is calculated for each point based on the deformation of the tracer mesh Φ (Lipinski & Mohseni 2010). Also, T represents the initial time at which the tracer particles are advected. Note that the direction of integration depends on the sign of τ and represents either a forward or backward FTLE when τ is positive or negative, respectively.

https://doi.org/10.1017/jfm.2013.532 Published online by Cambridge University Press

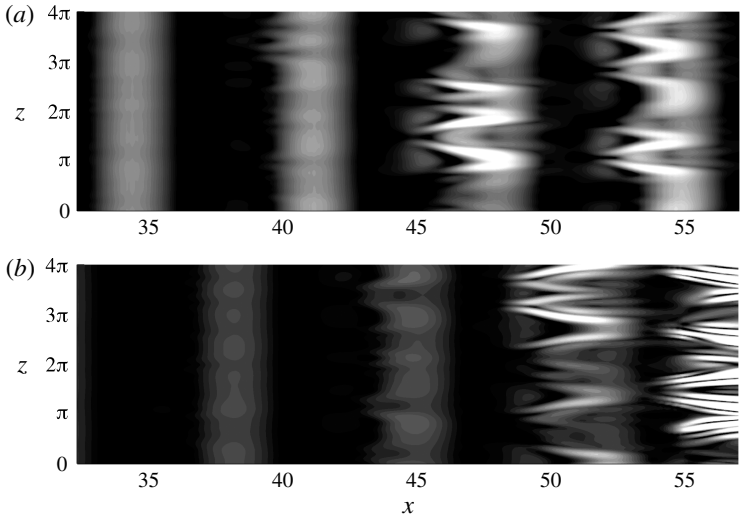


FIGURE 6. Two-dimensional forward FTLE fields in the critical layer $y \approx 1.88$ for the HA case at (*a*) $T = 225.3$ and (*b*) $T = 270.6$ for an integration time of $\tau = 0.357$.

It is important to note that the generation of LCS is a computationally demanding process. However, recent developments in ridge-tracking algorithms (Lipinski & Mohseni 2010) can alleviate this cost. Because FTLE fields define vortex boundaries (Shadden, Dabiri & Marsden 2006), they are ideally suited for use in the observation of Λ vortices in a direct numerical simulation. To this end, the integration time τ for the following LCS has been chosen such that coherent structures can be delineated with sharp boundaries and compare favourably with previous visualizations.

Forward FTLE fields for the HA case computed on an x–y plane at the critical layer $y \approx 1.88$ (where the mean flow and disturbance phase velocity are equal) at $T = 225.3$ and $T = 270.6$ for an integration time of $\tau = 0.357$ are presented in figure 6. In figure 6(*a*), the two-dimensional wave begins to break down into three-dimensional disturbances, forming clearly defined Λ vortices at $x \approx 45$, in a mostly staggered pattern, indicative of an H-type instability (Herbert 1983). The spanwise wavenumber of the Λ vortices varies between $2 \leqslant \beta \leqslant 3$ within $45 \leqslant x \leqslant 55$; these vortices stretch and distort as they convect downstream, as shown at $T = 270.6$ in figure 6(*b*). The similarity of these structures to previous experimental (Kozlov & Ramazanov 1983; Herbert 1988) and computational (Zang & Krist 1989; Saiki *et al.* 1993) visualizations of the Λ vortices is very strong, lending evidence for the LCS method to capture the characteristic structures in secondary instability. The integration time τ was selected to maximize the sharpness of the vortex boundaries.

Forward FTLE fields in the x–y plane taken at $z \approx 3.1$ are presented in figure 7 for $T = 248.1 \rightarrow 272.4$ and delineate two vortex lifting events (one at each wall) that are quasi-periodic and occur in a staggered fashion at the top and bottom walls of the channel. That is, the vortex lifting events at each wall are 180° out of phase with each other as a characteristic of H-type transition, where the high-shear layers localize and favour one wall (Herbert 1983; Saiki *et al.* 1993).

FTLE fields in the y–z plane taken at various streamwise locations at $T = 272.4$ are presented in figure 8 displaying vortical structures favouring either one wall or the other, depending on the streamwise location. It is not until $x \approx 57.1$ (figure 8*d*)

https://doi.org/10.1017/jfm.2013.532 Published online by Cambridge University Press

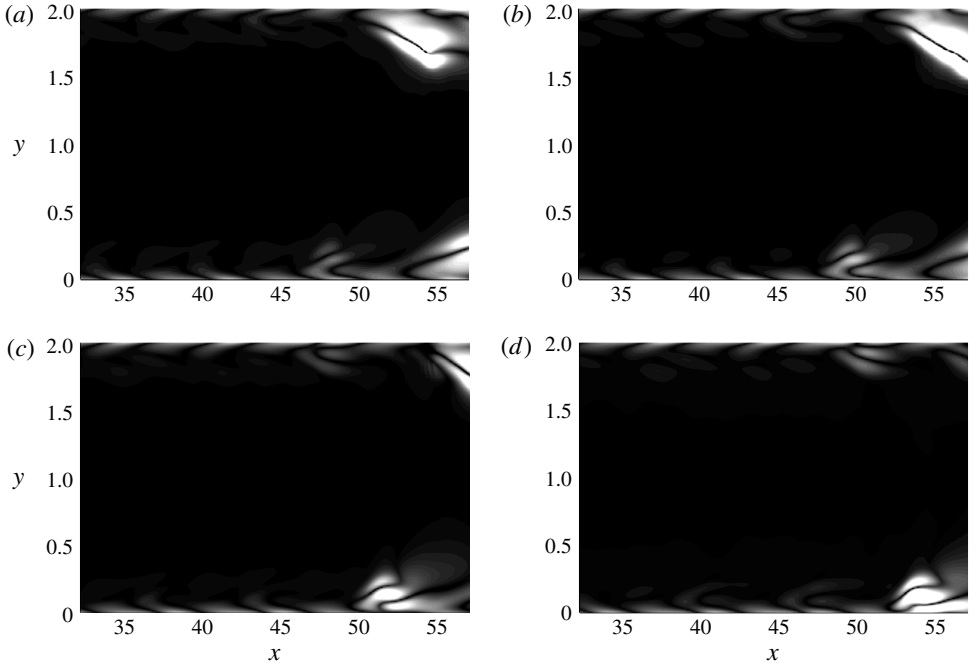


FIGURE 7. Two-dimensional forward FTLE fields at $z \approx 3.1$ for the HA case at (*a*) $T = 248.1$, (*b*) $T = 253.8$, (*c*) $T = 262.4$ and (*d*) $T = 272.4$ for an integration time of $\tau = 0.357$.

that the vortices on the bottom wall begin to lift up and form two distinct vortices manifesting large three-dimensional distortions with a spanwise wavenumber of $\beta \approx 2\beta_r$. It is interesting to note that these vortices appear to be biased in the spanwise direction, where the highest vorticity occurs from $y = 0 \rightarrow 2\pi$. It is evident from figure 8 that the disturbances switch from showing H-type characteristics (biasing on one wall) to K-type characteristics (no biasing) when travelling downstream. This is consistent with the streamwise evolution of the perturbation kinetic energy shown in figure 4(*b*), where H-type disturbances dominate throughout the length of the channel, until the amplitudes of the K-type (fundamental) modes approach those of the H-type near the end of the channel.

3.3. *Active control of transition*

Active control using suction/blowing has been demonstrated to significantly reduce the amplitude of the primary TS wave, thereby delaying transition as the phase between the streamwise and wall-normal velocity component is destroyed (Biringen 1984). Consequently, the perturbation field cannot transfer energy from the mean motion since the major production term in the turbulent energy equation, $\overline{u'v'}\,\partial U/\partial y$ is reduced (Biringen 1984; Danabasoglu *et al.* 1991), where the overline denotes a time average. In previous work regarding suction/blowing, the inflow conditions specified either H- or K-type secondary disturbances (Biringen, Nutt & Caruso 1987) or were explicitly two-dimensional (Erdmann *et al.* 2011). In the present case, the secondary instability is allowed to evolve naturally with no *a priori* assumptions on its structure. In this section we demonstrate the applicability of transition delay using suction/blowing to attenuate the primary mode and, consequently, the secondary modes in a simulated 'natural' instability environment.

https://doi.org/10.1017/jfm.2013.532 Published online by Cambridge University Press

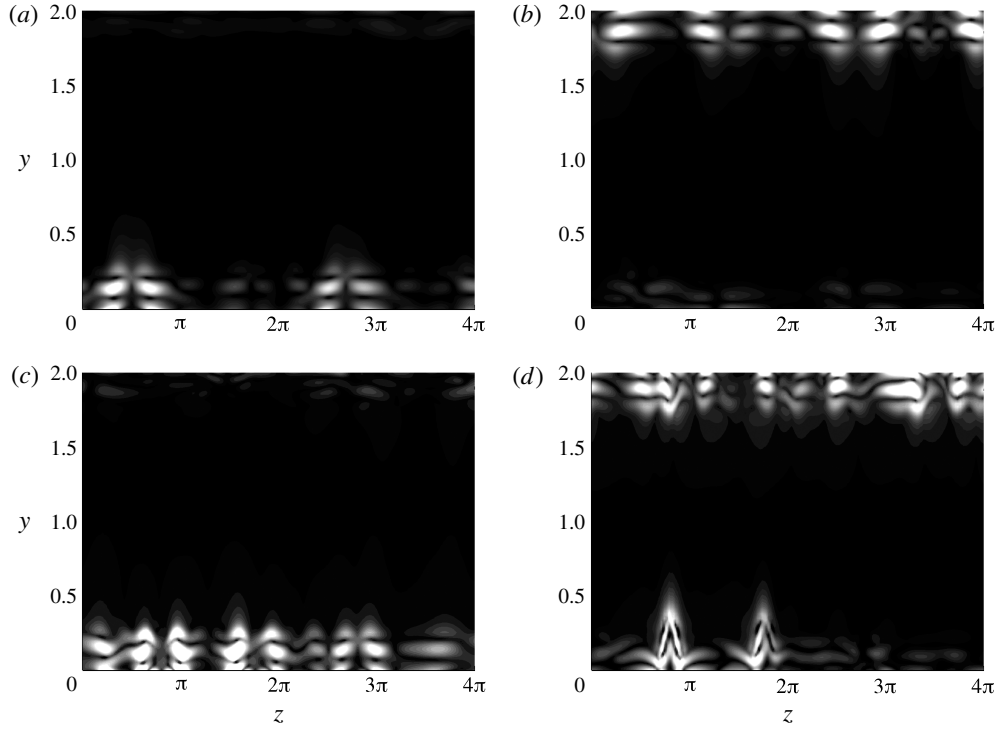


FIGURE 8. Two-dimensional forward FTLE fields in the y–z plane at $T = 272.4$ for the HA case at (*a*) $x \approx 47.3$, (*b*) $x \approx 50.6$, (*c*) $x \approx 53.85$ and (*d*) $x \approx 57.1$ for an integration time of $\tau = 0.357$.

Active control of the LA case was initiated using a spanwise-homogeneous suction/blowing slot located at $x_s = 21.58$ and $x_e = 22.77$. The amplitude of the control signal was set to $A_c = 5.69 \times 10^{-3}\, U_c$, and corresponds to the suggested value of Biringen (1984), where this amplitude (as the sum of both walls) must be about twice the amplitude of the wall-normal velocity component. The phase of the control wave for the LA case was determined by trial and error until attenuation of the primary mode was observed. Evidence of transition delay for the LA case is presented in figure 9(*a*), where the vertical lines denote the start ($x_s = 21.58$) and end ($x_e = 22.77$) of the suction/blowing slot, with the streamwise length of this slot set approximately as 20 % of the primary TS wave (Danabasoglu *et al.* 1991). There is a slight upstream influence of the suction/blowing slot, with an increase in the total energy at the slot centre, and then a rapid decrease in the total energy downstream of the slot owing to the destruction of phase between u' and v'. Further downstream of the slot, the two velocity components again become phase-locked, which produces a linear increase in the total energy along the channel. This is in agreement with previous active control cases (Biringen 1984; Danabasoglu *et al.* 1991), where, after an initial adjustment, the energy in the flow would again increase linearly downstream of the suction/blowing slot. Near the end of the channel $x = 45$, there is a $\Delta E_{\%} = 57\,\%$ decrease in the primary $(1, 0)$ mode when compared to the uncontrolled LA case (figure 4*a*). In addition, the amplitudes of the secondary modes are redistributed, with a more 'mixed' secondary instability as indicated by the similar amplitudes of the

https://doi.org/10.1017/jfm.2013.532 Published online by Cambridge University Press

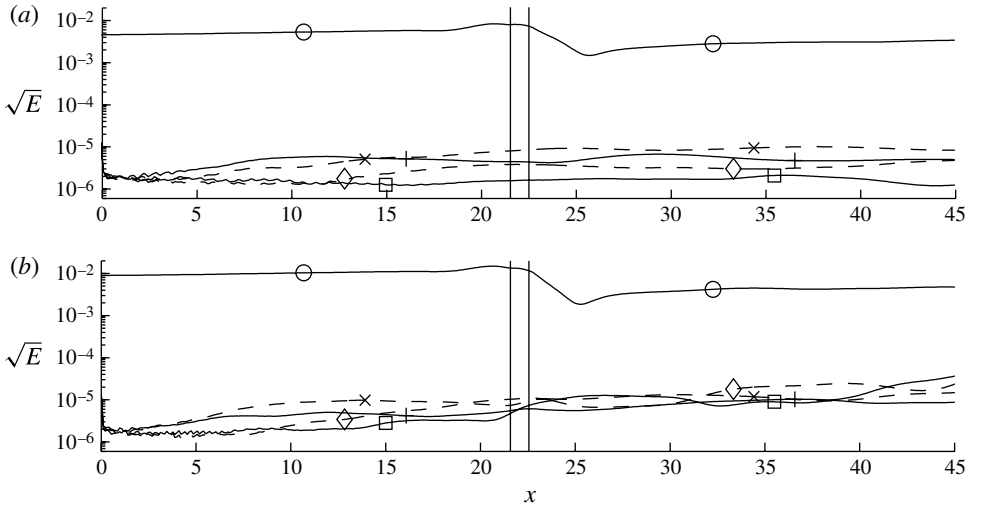


FIGURE 9. Streamwise evolution of integrated kinetic energy for specific modes for two cases. (*a*) Case LA: ∘, (1, 0); ◇, (0.5, 1); ×, (0.5, 2.5); □, (1, 1); +, (1, 2.5). (*b*) Case HA: ∘, (1, 0); ◇, (0.5, 1.5); ×, (0.5, 4); □, (1, 1.5); +, (1, 4). Solid lines represent fundamental modes, while dashed lines represent subharmonic modes.

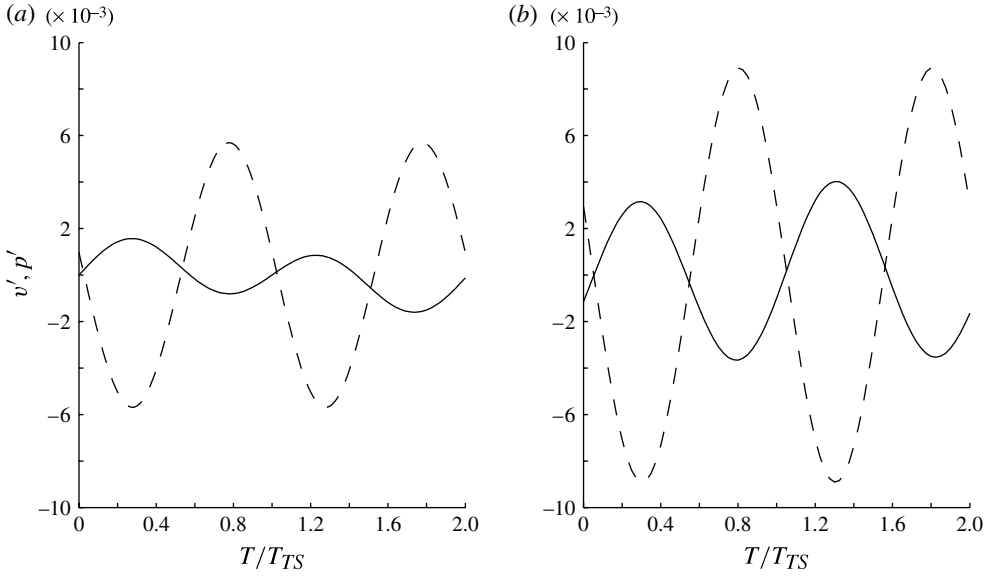


FIGURE 10. Wall-normal control signal measured at the suction/blowing slot (dashed line) and the wall pressure signal (solid line) measured at $x = 18.77$ over two full TS periods for (*a*) case LA and (*b*) case HA.

subharmonic (dashed lines) and fundamental (solid lines) modes when compared to the overall higher H-type secondary mode observed without control in figure 4(*a*).

As mentioned earlier, the phase angle ϕ of the control signal was determined through trial and error, much like in Danabasoglu *et al.* (1991). However, by measuring the local wall pressure at some fixed location upstream of the suction/blowing slot, one can 'tune' the phase angle such that the phase shift between

https://doi.org/10.1017/jfm.2013.532 Published online by Cambridge University Press

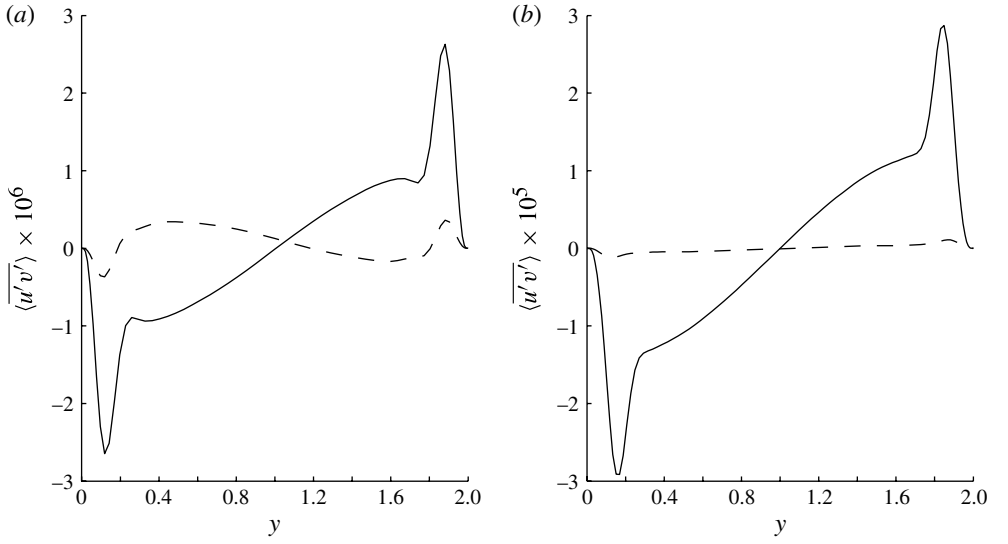


FIGURE 11. The $\langle \overline{u'v'} \rangle$ distributions at $x = 45$ for (a) case LA and (b) case HA: solid line, no control; dashed line, with control.

the measured pressure signal and the control signal (ϕ_{shift}) will properly attenuate the TS wave. This is demonstrated for the LA case in figure 10(a), where the wall pressure was sampled at a fixed location at $x = 18.77$. Note that, at this particular location, the wall control signal is 180° out of phase with the wall pressure. We apply this same control strategy for the HA case by measuring the pressure at this same location and ensuring that the control signal is 180° out of phase with this pressure signal, which is shown in figure 10(b).

The results of this control strategy for the HA case, with the control amplitude $A_c = 8.92 \times 10^{-3}\, U_c$, is provided in figure 9(b) and show similar attenuation of the primary mode from the suction/blowing slot as the LA case. There is approximately a $\Delta E_{\%} = 72\,\%$ decrease in the primary $(1, 0)$ mode when compared to the uncontrolled HA case at $x = 45$. All of the secondary modes have also decreased significantly in amplitude when compared to the uncontrolled case (figure 4b), where a mixing of fundamental and subharmonic modes is present. Again, some distance away from the control slot, the streamwise and wall-normal velocity components become phase-locked and begin to transfer energy into the primary mode. This may be circumvented by arranging a series of these two-dimensional suction/blowing slots along the streamwise direction, with each slot tuned to the correct phase angle ϕ to attenuate the TS wave.

Temporally averaged shear stress distributions, averaged over the channel width $\langle \overline{u'v'} \rangle$, are presented in figure 11 at $x = 45$. For both the LA and HA cases, the distributions clearly display a mitigation of the shear stress across the channel. It is interesting to note that the control is less effective for low-amplitude disturbances compared to the high-amplitude case, where the phase angles between the pressure and wall signals (figure 10) for both cases were equal. In addition, the control amplitude A_c for both cases was set to equal that of the wall-centred uncontrolled velocity for each case, as suggested by Biringen (1984). Consequently, this difference may be attributed to the magnitude of the three-dimensional perturbation streamwise velocity u'_{3D} compared to the two-dimensional velocity u'_{2D}, which is represented by A_{3D} and

https://doi.org/10.1017/jfm.2013.532 Published online by Cambridge University Press

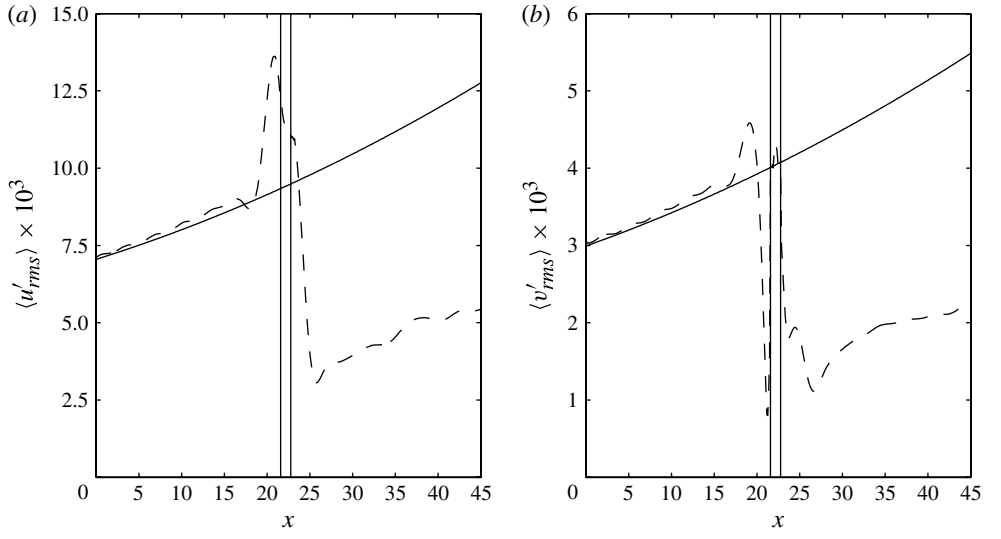


FIGURE 12. Case LA streamwise evolution of (*a*) $\langle u'_{rms}\rangle$ and (*b*) $\langle v'_{rms}\rangle$: solid line, no control; dashed line, with control.

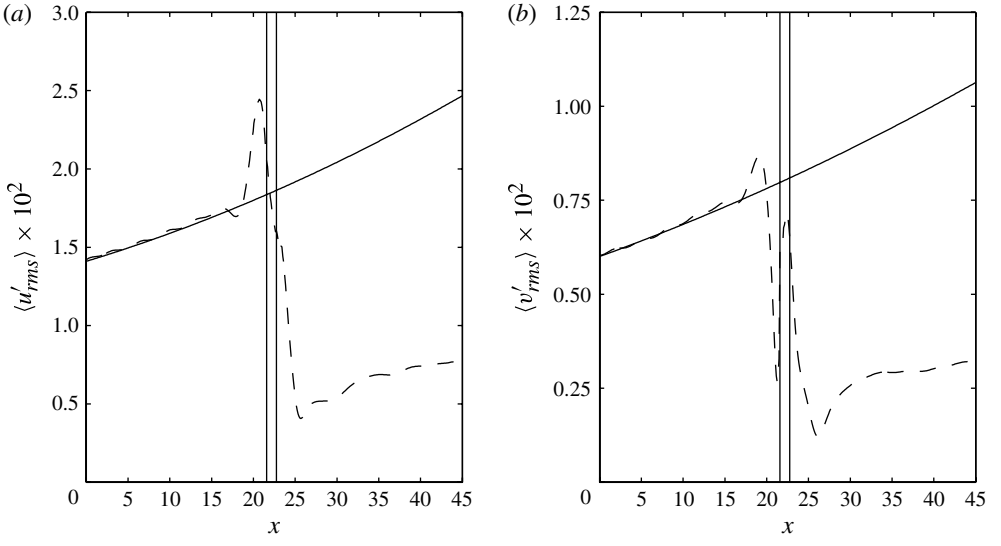


FIGURE 13. Case HA streamwise evolution of (*a*) $\langle u'_{rms}\rangle$ and (*b*) $\langle v'_{rms}\rangle$: solid line, no control; dashed line, with control.

A_{2D} in table 1. At the inflow for the LA case, the ratio u'_{2D}/u'_{3D} is twice that of the HA case. This indicates that the optimum control amplitude may deviate from the wall-centred uncontrolled velocity when the three-dimensional component of the disturbances approach that of the two-dimensional components.

Spatial distributions of maximum root mean squared (r.m.s.) streamwise and spanwise perturbation velocities, spatially averaged across the span of the channel,

https://doi.org/10.1017/jfm.2013.532 Published online by Cambridge University Press

Case	$\frac{A_{2D}}{U_c}$	$\frac{A_c}{U_c}$	ϕ_{shift} (deg.)	$\Delta E_{\%}$ (%)	$\frac{E_D}{E_S}$
LA	0.01	5.69×10^{-3}	180	57	1.43
HA	0.02	8.92×10^{-3}	180	72	2.42

TABLE 2. Summary of control cases for $Re = 10\,000$.

are given in figures 12 and 13 for the LA and HA cases, respectively. The edges of the suction/blowing slot are noted by straight vertical lines, and $\langle \quad \rangle$ denotes a spatial average in the spanwise direction. Observed is an upstream-travelling wave due to the presence of the suction/blowing slot, which initially increases the amplitudes of $\langle u'_{rms} \rangle$ and $\langle v'_{rms} \rangle$ and decays rapidly as the wave propagates upstream, in accordance with the experimental observations of Ashpis & Reshotko (1990). Downstream of the slot, $\langle u'_{rms} \rangle$ and $\langle v'_{rms} \rangle$ for both cases show a substantial reduction in amplitude and then begin to grow again, albeit at a slower rate than for the cases without control.

In order for this control method to be applicable, the amount of energy supplied to the actuating control slot must be lower than the energy saved using the control strategy. For a constant mass flow rate, any change in the wall shear stress, and consequently in the coefficient of drag, must manifest itself in a corresponding change in the pressure gradient (Chang *et al.* 2002). This metric is usually used in a fully turbulent flow, where the shear stress changes are large between control and no-control cases, and therefore the change in pressure gradients are also large. However, the current flow is transitional, with the perturbations small compared to the mean flow, which implies very small changes in the pressure gradient. Because our aim is to delay transition with this control strategy, a better measure is the amount of decrease in the amplitude of the $(1, 0)$ mode in E (equation (3.1)) for a controlled case compared to an uncontrolled case, averaged from the start of the control slot to the end of the physical domain, defined as

$$E_D = \frac{1}{(L_x - x_s)} \int_{x_s}^{L_x} (E^{nc} - E^{wc})\, \mathrm{d}x, \tag{3.3}$$

where E^{nc} and E^{wc} are the vertically averaged kinetic energies (equation (3.1)) of the $(1, 0)$ mode for the no-control (nc) and with-control (wc) cases. These modal distributions have already been presented in figures 4 and 10. The average energy that must be supplied to the control slot is given by

$$E_S = \lim_{T \to \infty} \frac{2}{T} \int_{t_0}^{t_0+T} (\boldsymbol{u} \cdot \boldsymbol{n})^2\, \mathrm{d}t, \tag{3.4}$$

where $\boldsymbol{u}$ is the control slot velocity given in (2.5) and $\boldsymbol{n}$ is the outward unit normal from the control slot located at the channel walls. The factor of two accounts for the slot that is located at the top and bottom walls. The energy ratio of E_D to E_S then can be used as a measure for the efficiency of this control strategy. This ratio and a summary of the flow control results are presented in table 2.

The energy ratios for the LA and HA cases are 1.43 and 2.42, respectively. Because these quantities are greater than unity, the energy saved is greater than the energy expended in actuating the control slot. Note that it was assumed that there were no losses from the actuators, so these are 'ideal' quantities. However, in a real application,

https://doi.org/10.1017/jfm.2013.532 Published online by Cambridge University Press

the control wave amplitude can be adjusted until an optimal reduction in the primary mode is achieved.

4. Conclusions

This paper has presented the results of a spatially evolving plane-channel flow with a constant pressure gradient, subject to two-dimensional disturbances superimposed with random noise at the inflow. It was shown that, for low amplitudes $A_{2D} = 0.01U_c$, the flow has a bias towards H-type modes with relatively modest growth in the secondary modes ($O(10^1)$), in agreement with the theory of Herbert (1983). For high amplitudes $A_{2D} = 0.02U_c$, initially there is biasing towards the H-type modes, with the K-type modal amplitudes approaching that of the H-type modes as the disturbances travel downstream. In addition, much larger growth in the secondary modes was observed in the HA case ($O(10^3)$) compared to the LA case, despite the initial two-dimensional amplitude for the HA case being only a factor of two larger. The present high-resolution spatial results verify and confirm previous periodic temporal numerical simulations (Singer *et al.* 1989). However, in contrast to the results of Kim & Moser (1989), K-type dominated transition was not observed for either the LA or HA case.

Forward FTLE fields were used to generate LCS to visualize characteristic Λ vortices as well as vortex lifting events commonly present in a secondary instability transition scenario. The LCS presented here show qualitative agreement with previous experimental and computational visualizations, and represent a viable means of flow visualization in a transitional flow field.

Finally, it was shown that the control of the LA and HA cases was possible using a suction/blowing slot located at a fixed streamwise location and introducing a two-dimensional control wave at the fundamental TS frequency. The phase of this control wave is determined by measuring the wall pressure at a fixed location upstream of the suction/blowing slot, where the signal is time-lagged with respect to the wall pressure signal. For this case, a substantial reduction in the integrated kinetic energy of the primary mode downstream of the slot was observed. The r.m.s. distributions of streamwise and wall-normal velocity show large reductions in their amplitudes downstream of the control slot, effectively delaying transition when compared to the LA case with no control. This method was also shown to be efficient, as the energy that must be supplied to the actuator of the suction/blowing slot is lower than the energy saved for both low- and high-amplitude three-dimensional disturbances.

Acknowledgements

This work was supported by NSF-IDR Award No. 1131802. Computational resources were provided by NSF on the Kraken supercomputer at the National Institute for Computational Sciences. Algorithms for generation of FTLE fields, along with helpful discussions, were provided by Dr D. Lipinski. The authors thank the anonymous referees for their careful reading of the manuscript and their very helpful comments.

REFERENCES

ASHPIS, D. & RESHOTKO, E. 1990 The vibrating ribbon problem revisited. *J. Fluid Mech.* **213**, 531–547.

BARKLEY, D. 1990 Theory and predictions of finite-amplitude waves in two-dimensional plane Poiseuille flow. *Phys. Fluids* A **6**, 955–970.

https://doi.org/10.1017/jfm.2013.532 Published online by Cambridge University Press

BAUMANN, M. & NITSCHE, W. 1996 Investigation of active control of Tollmien–Schlichting waves on a wing. *Trans. Bound. Layer Aeronaut.* **46**, 89–98.

BIRINGEN, S. 1984 Active control of transition by periodic suction–blowing. *Phys. Fluids* **27** (6), 1345–1347.

BIRINGEN, S., NUTT, W. E. & CARUSO, M. J. 1987 Numerical study of transition control by periodic suction blowing. *AIAA J.* **25** (2), 239–244.

BORODULIN, V. I., KACHANOV, Y. S. & KOPTSEV, D. B. 2002 Experimental study of resonant interactions of instability waves in a self-similar boundary layer with an adverse pressure gradient: I. Tuned resonances. *J. Turbul.* **3**, N62.

CHANG, Y., COLLIS, S. & RAMAKRISHNAN, S. 2002 Viscous effects in control of near-wall turbulence. *Phys. Fluids* **14**, 4069–4080.

CHOI, H., MOIN, P. & KIM, J. 1994 Active turbulence control for drag reduction in wall-bounded flows. *J. Fluid Mech.* **262**, 75–110.

DANABASOGLU, G., BIRINGEN, S. & STREETT, C. L. 1991 Spatial simulation of instability control by periodic suction blowing. *Phys. Fluids* A **3** (9), 2138–2147.

ERDMANN, R., PATZOLD, A., ENGERT, M., PELTZER, I. & NITSCHE, W. 2011 On active control of laminar–turbulent transition on two-dimensional wings. *Phil. Trans. R. Soc. Lond.* A **369**, 1382–1395.

HALLER, G. 2002 Lagrangian coherent structures from approximate velocity data. *Phys. Fluids* **14**, 1851–1861.

HERBERT, T. 1983 Secondary instability of plane channel flow to subharmonic three-dimensional disturbances. *Phys. Fluids* **26**, 871–874.

HERBERT, T. 1988 Secondary instability of boundary layers. *Annu. Rev. Fluid Mech.* **20**, 487–526.

KACHANOV, Y. S., KOZLOV, V. V. & LEVCHENKO, V. Y. 1978 Nonlinear development of a wave in a boundary layer. *Fluid Dyn.* **12**, 383–390.

KACHANOV, Y. S. & LEVCHENKO, V. Y. 1984 The resonant interaction of disturbances at laminar–turbulent transition in a boundary layer. *J. Fluid Mech.* **138**, 209–247.

KIM, J. & MOSER, R. D. 1989 On the secondary instability in plane Poiseuille flow. *Phys. Fluids* A **1** (5), 775–777.

KLEBANOFF, P. S., TIDSTROM, K. D. & SARGENT, L. M. 1962 The three-dimensional nature of boundary-layer instability. *J. Fluid Mech.* **12**, 1–34.

KOZLOV, V. V. & RAMAZANOV, M. P. 1983 Development of finite-amplitude disturbances in Poiseuille flow. *J. Fluid Mech.* **147**, 149–157.

KRUSE, M. & WAGNER, S. 1998 Visualization and laser Doppler measurements of the development of Lambda vortices in laminar–turbulent transition. *Meas. Sci. Technol.* **9**, 659–669.

LIPINSKI, D. & MOHSENI, K. 2010 A ridge tracking algorithm and error estimate for efficient computation of Lagrangian coherent structures. *Chaos* **20**, 017504.

MAY, C. L. & KLEISER, L. 1985 Numerical simulation of subharmonic transition in plane Poiseuille flow. *Bull. Am. Phys. Soc.* **30**, 1748.

NISHIOKA, M., ASAI, M. & IIDA, S. 1980 An experimental investigation of the secondary instability. In *Laminar–Turbulent Transition: Proc. IUTAM Symp., Stuttgart, West Germany, 16–22 September 1979* (ed. R. Eppler & H. Fasel), pp. 37–46. Springer.

NISHIOKA, M., IIDA, S. & ICHIKAWA, Y. 1975 An experimental investigation of the stability of plane Poiseuille flow. *J. Fluid Mech.* **72**, 731–751.

RAMAZANOV, M. P. 1985 Development of finite-amplitude disturbances in Poiseuille flow. In *Laminar–Turbulent Transition: Proc IUTAM Symp., Novosibirsk, USSR, 9–13 July 1984* (ed. V. V. Kozlov), pp. 183–190. Springer.

REYNOLDS, W. C. 1969 Orrsom: A Fortran-IV program for solution of the Orr–Sommerfeld equation. *Tech. Rep.* FM-4. Stanford University.

SAIKI, E. M., BIRINGEN, S., DANABASOGLU, G. & STREETT, C. L. 1993 Spatial simulation of secondary instability in plane channel flow: comparison of K- and H-type disturbances. *J. Fluid Mech.* **253**, 485–507.

SARIC, W. S., KOZLOV, V. V. & LEVCHENKO, V. Y. 1984 Forced and unforced subharmonic resonance in boundary layer transition. *AIAA Paper* 84-0007.

https://doi.org/10.1017/jfm.2013.532 Published online by Cambridge University Press

SHADDEN, S. C., DABIRI, J. O. & MARSDEN, J. E. 2006 Lagrangian analysis of fluid transport in empirical vortex ring flows. *Phys. Fluids* **18**, 047105.

SHADDEN, S. C., LEKIEN, F. & MARSDEN, J. E. 2005 Definition and properties of Lagrangian coherent structures from finite-time Lyapunov exponents in two-dimensional aperiodic flows. *Physica* D **212**, 271–304.

SHADDEN, S. C., LEKIEN, F., PADUAN, J. D., CHAVEZ, F. P. & MARSDEN, J. E. 2009 The correlation between surface drifters and coherent structures based on high-frequency radar data in Monterey Bay. *Deep-Sea Res.* II **56**, 161–172.

SINGER, B. A. 1987 Numerical simulation studies of laminar–turbulent transition in the plane channel. PhD thesis, Stanford University, CA.

SINGER, B. A., REED, H. L. & FERZIGER, J. H. 1989 The effects of streamwise vortices on transition in the plane channel. *Phys. Fluids* **1**, 1960–1971.

SPALART, P. R. & YANG, K. S. 1987 Numerical study of ribbon-induced transition in Blasius flow. *J. Fluid Mech.* **178**, 345–365.

VOTH, G. A., HALLER, G. & GOLLUB, J. P. 2002 Experimental measurements of stretching fields in fluid mixing. *Phys. Rev. Lett.* **88**, 254501.

WAGGY, S., BIRINGEN, S. & SULLIVAN, P. P. 2013 Direct numerical simulation of top-down and bottom-up diffusion in the convective boundary layer. *J. Fluid Mech.* **724**, 581–606.

ZANG, T. A. & KRIST, S. E. 1989 Numerical experiments on stability and transition in plane channel flow. *Theor. Comput. Fluid Dyn.* **1**, 41–64.

https://doi.org/10.1017/jfm.2013.532 Published online by Cambridge University Press